AIAA JOURNAL
Vol. 47, No. 12, December 2009

Numerical Prediction of Exhaust Fan-Tone Noise from High-Bypass Aircraft Engines

Anupam Sharma,* Simon K. Richards,* Trevor H. Wood,* and Chingwei Shieh†
General Electric Global Research Center, Niskayuna, New York 12309

DOI: 10.2514/1.42208

The ability to accurately predict fan noise is important in designing and optimizing high-bypass aircraft engines for low noise emissions. In this paper, a prediction methodology for exhaust fan-tone noise analysis is described and validated against various canonical test cases and NASA Source Diagnostic Test data (Heidelberg, L. J., "Fan Noise Source Diagnostic Test—Tone Modal Structure Results," NASA TM–2002-211594, 2002.). The prediction process consists of solving Reynolds-averaged Navier–Stokes equations to compute the fan wake and calculating the acoustic response of the outlet guide vanes to the fan wake using linearized Euler equations. Very good agreement is observed between the numerical predictions and semi-analytical results for canonical cases. Detailed comparisons against the Source Diagnostic Test data are presented for unsteady vane pressure and integrated in-duct exhaust noise power levels. Geometric trends for different outlet guide vane configurations at various operating conditions are also analyzed and found to be in good agreement with data.

Nomenclature

$a_{m,n}$	=	complex amplitude of the (m, n) mode
C_p	=	coefficient of pressure
c	=	speed of sound
j	=	$\sqrt{-1}$
k_z	=	complex wave number in the axial direction
m	=	circumferential mode number
N_B	=	number of rotor blades
N_V	=	number of stator vanes
n	=	radial mode number
P_{ref}	=	reference acoustic pressure, 20 μPa
PWL_{ref}	=	reference acoustic power, 10^{-12} W
r_H	=	hub radius
r_T	=	tip radius
U	=	column vector of primitive flow variables
$\sum$	=	sum of radial mode power levels
ϕ	=	phase of a complex variable
$\psi_{m,n}$	=	eigenvector corresponding to the (m, n) mode
Ω	=	rotor shaft rotation rate, rad/s

Superscripts

(a)	=	$\bar{\rho}^{-1}(p' + \bar{\rho}\bar{v}_z v'_z)$
(b)	=	$\bar{\rho}v'_z + p'\bar{v}_z$
(PS)	=	pressure side
$\bar{Q}$	=	time average of variable Q
Q'	=	perturbation of Q about $\bar{Q}$
(SS)	=	suction side

I. Introduction

ROTOR–STATOR interaction tone noise, often referred to as "fan-tone" noise, is a major source of annoyance in high-bypass-ratio aircraft engines. This noise source is especially prominent at low-speed conditions, when fan noise typically dominates over jet noise. Fan-tone noise is a result of periodic interaction of the rotor wake with the downstream stators [outlet guide vane (OGV) or strut]. During this interaction, the vortical energy in the wake is converted into acoustic energy that radiates both upstream and downstream. Although the upstream traveling acoustic waves are partially blocked (and scattered) by the rotor, the downstream traveling waves propagate down the duct relatively unimpeded and radiate through the exhaust.

The phenomenon of fan-tone-noise generation falls into the general category of unsteady flows through blade rows of axial flow turbomachinery. There are three major approaches to study such problems, viz., classical semi-analytical methods, linearized computational analyses, and nonlinear time-marching computational aeroacoustics (CAA) methods. Small harmonic perturbation assumptions are made in the linearized analyses to obtain a system of equations in the frequency domain. It is generally accepted [1,2] that these assumptions are valid for the prediction of fan-tone noise. Classical analyses further simplify the problem by assuming a uniform background flow. Nonlinear time-marching CAA methods directly solve for the entire flow and acoustic fields by marching solutions forward in time. These methods are typically very computationally intensive and, therefore, not suitable for design purposes.

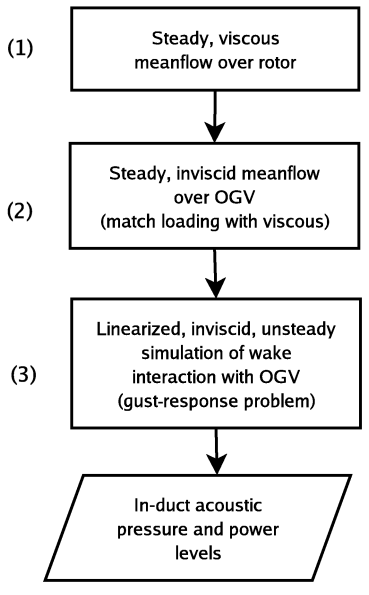

Fig. 1 Flowchart illustrating the fan-tone noise prediction process.

Presented as Paper 3700 at the 13th AIAA/CEAS Aeroacoustics Conference (28th AIAA Aeroacoustics Conference), Rome, Italy, 21–23 May 2007; received 14 November 2008; revision received 1 August 2009; accepted for publication 2 August 2009.

*Mechanical Engineer, 1 Research Circle. Member AIAA.
†Fluid Mechanics Engineer, 1 Research Circle. Member AIAA.

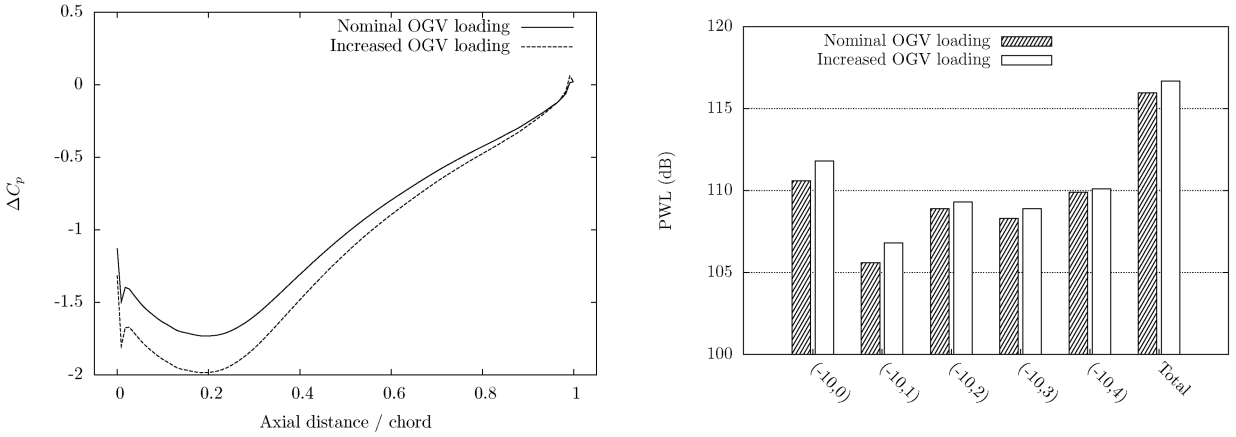

a) ΔC_p **b) PWL (dB)**

Fig. 2 Effect of OGV mean loading on fan-tone noise: a) two different loading profiles, and b) corresponding exhaust acoustic mode power levels.

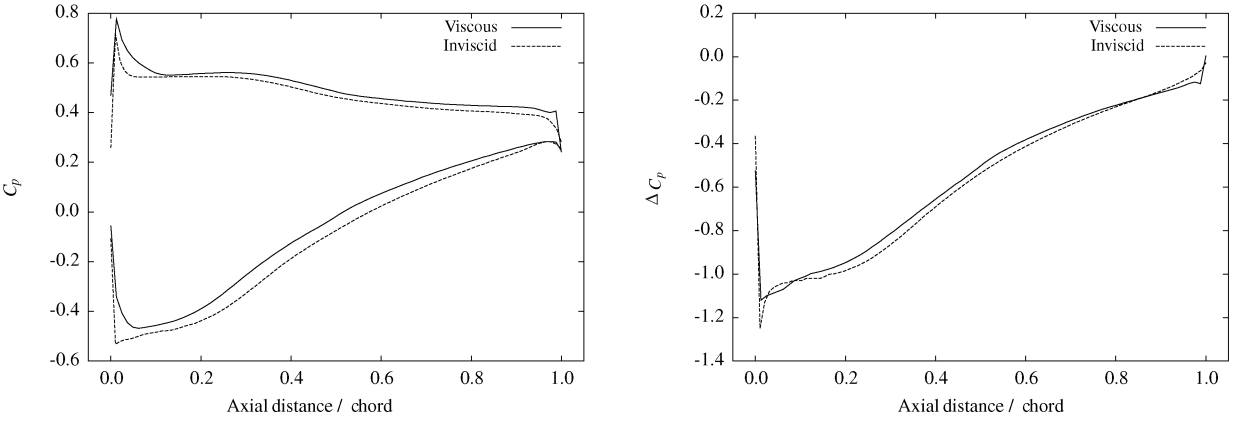

a) C_p **b) ΔC_p**

Fig. 3 Sample comparison of inviscid versus viscous steady loading on an OGV (90% span): a) C_p, and b) $\Delta C_p = C_p^{SS} - C_p^{PS}$.

Classical analyses are computationally inexpensive but they may not be representative of realistic turbomachinery flow as the background flow in the region between the rotor and the vane is highly nonuniform. Linearized analyses can serve to meet the challenges of detailed blade design by providing a compromise between accuracy and computation time.

Examples of classical methods include the 2-D flow analysis by Smith [3] and the semi-analytical lifting line and lifting surface methods of Namba [4], Namba and Schulten [5], and Schulten [6,7]. Linearized Euler equations were numerically solved for two-dimensional flows in the potential-based cascade analyses of Whitehead [8] and Hall and Verdon [9]. An extension of this approach to 3-D flows was presented by Prasad and Verdon [10], who analyzed wake–stator interaction for flat-plate cascades. This approach has also been used to assess the acoustic benefit of sweep and lean in stator vanes. A similar approach was taken by Atassi et al. [11,12] to study scattering of vortical and acoustic disturbances by annular cascades. Envia et al. [13] performed a parametric study

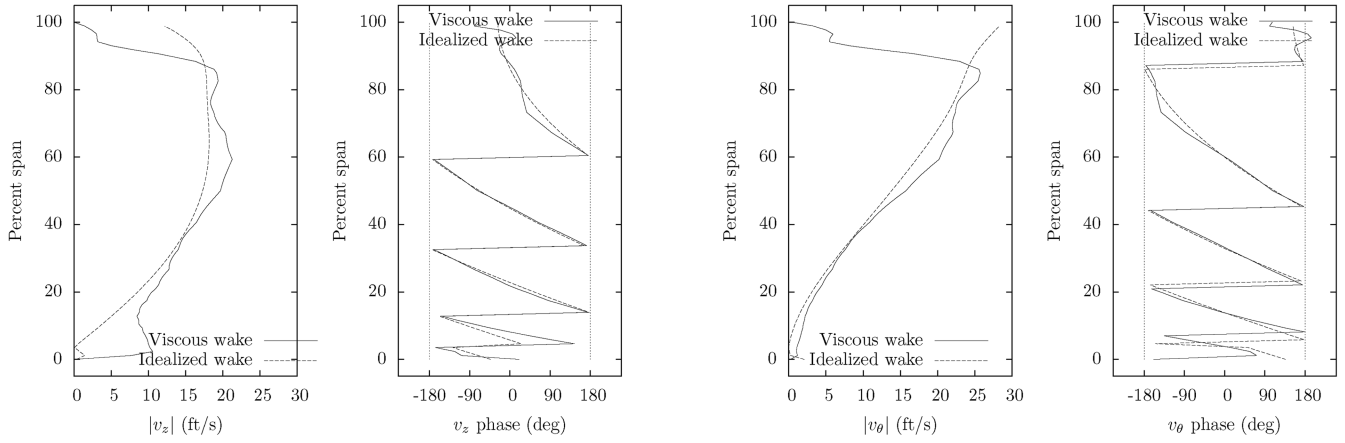

a) Axial velocity **b) Circumferential velocity**

Fig. 4 Spanwise variation of wake gust velocity components.

Table 1 Parameters for flat-plate cascade validation

Parameter	Value
N_B	16
N_V	24
$\bar{v}_z$	1.0
c	2.0
n	1
a_1	$1 + 0i$

Table 2 Parameters for 2-D flat-plate cascade validation

Case	M_t	ω
a	0.3897	3.2648
b	0.4330	3.6276
c	0.4763	3.9903
d	0.6495	5.4413
e	1.5000	12.5664
f	2.5980	21.7650

involving a stripwise analysis of wake–stator interaction coupled with a 3-D duct Green's function to estimate in-duct noise levels. In the present work, 3-D linearized Euler equations are solved for harmonic perturbations about nonuniform background flow to predict fan-tone noise for a realistic fan configuration. Three stator geometries are investigated, and the results are compared against experimental data.

The following section describes the noise prediction process used in this work. Section III presents a validation of the process against semi-analytical results for canonical problems. Section IV presents comparisons of the numerical predictions against NASA Source Diagnostic Test (SDT) experimental data. Comparisons are made for vane unsteady surface pressure and modal exhaust sound power levels, as well as geometric trends for the three different OGV configurations.

II. Noise Prediction Process

Figure 1 shows a flowchart of the numerical prediction process used in the present work. It consists of three steps: 1) calculation of the rotor wake by solving the viscous mean flow over the rotor, 2) calculation of background mean flow over the OGV, and 3) simulation of wake impinging on the OGV.

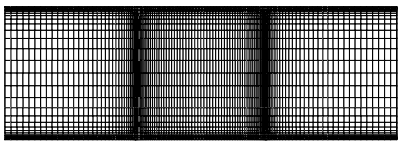

Fig. 5 Grid used to calculate the gust response of a narrow-annulus flat-plate cascade. Every other point is omitted for clarity.

The first step of the process involves the solution of Reynolds-averaged Navier–Stokes (RANS) equations (in the rotor frame of reference) to obtain the velocity defect in the wake of the rotor. A two-equation k–ω turbulence model is employed to correctly capture the mean velocity defect in the wake. Numerically computed wakes are used for the results presented in this paper, although experimentally obtained wake profiles can also be employed with the procedure outlined.

In the second step, the viscous mean flow over the OGV is calculated to ensure correct operating conditions in the simulation. An equivalent inviscid mean flow, approximately matching the vane loading with the viscous solution, is then obtained by tuning the inlet boundary conditions. The parameters typically modified to achieve this load matching are inlet total pressure and incidence angle; typically, a few iterations are required to obtain a suitable solution. Although it is impossible to get an exact match in the loading distribution between the viscous and inviscid solutions, it is important to minimize the difference as the mean vane loading distorts the incoming gust, which changes the radiated noise. To assess the impact of the mean loading error on noise prediction, two cases with about a 12% difference in mean vane loading were run. The difference in exhaust acoustic power level was found to be less than 0.75 dB; see Fig. 2. The difference in mean OGV loading between the viscous and inviscid calculations was less than 10% for all cases considered here.

Figure 3 shows a sample comparison of a load-matched inviscid solution versus the original viscous solution. Note that the coefficient of pressure (C_p) profiles for the inviscid solution are shifted down with respect to the viscous solution, but the loading (ΔC_p) matches well.

The third step of the process requires a gust-response simulation using the linearized unsteady Euler equations (see the Appendix). The problem is formulated and solved in the frequency domain with focus on the harmonics of the blade-passing frequency (BPF). A modified formulation of the three-dimensional nonreflecting boundary conditions developed by Verdon [2] is used in this analysis; the details are available in the Appendix. The Appendix also presents a validation of the numerical solution of the eigensystem.

An inviscid representation of the wake is sought as input to the gust-response calculation. The end-wall boundary layer and tip vortex effects are removed from the wake profile by smoothly extrapolating it in the radial direction near the hub and tip. The inviscid wake is referred to as the "idealized" wake. The wake defect is calculated by subtracting the circumferentially averaged mean flow from the idealized wake. A spatial Fourier transformation in the circumferential direction is then performed at each radial grid location to decompose the wake into BPF harmonics. For a constant rotor rotation rate, the circumferential Fourier transform in the rotor reference frame is equivalent to a temporal Fourier transform in the stationary frame. A sample comparison of the first BPF harmonic of the viscous and the idealized wake profiles is provided in Fig. 4.

The harmonic representation of the idealized wake profile is applied as a perturbation (gust) at the inlet boundary for the linear unsteady calculation. This perturbation is convected downstream by the mean flow, where it interacts with the OGV, generating upstream and downstream propagating acoustic waves.

Finally, a 3-D acoustic mode decomposition is performed at the exit boundary of the computational domain, and the sound pressure

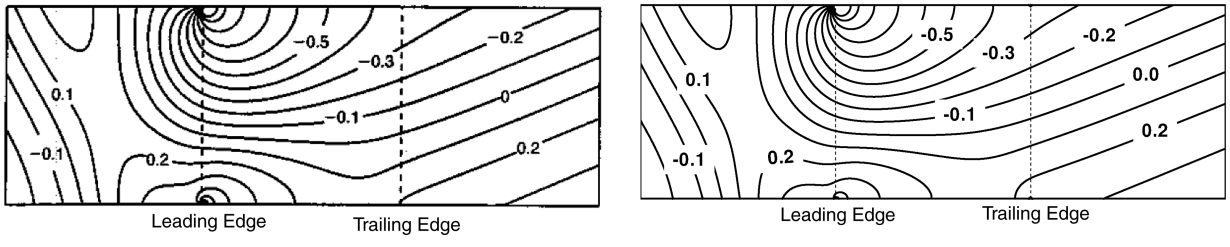

Fig. 6 Contours of imaginary part of unsteady pressure for the $M_t = 0.65$ case: a) classical results [23], and b) numerical results.

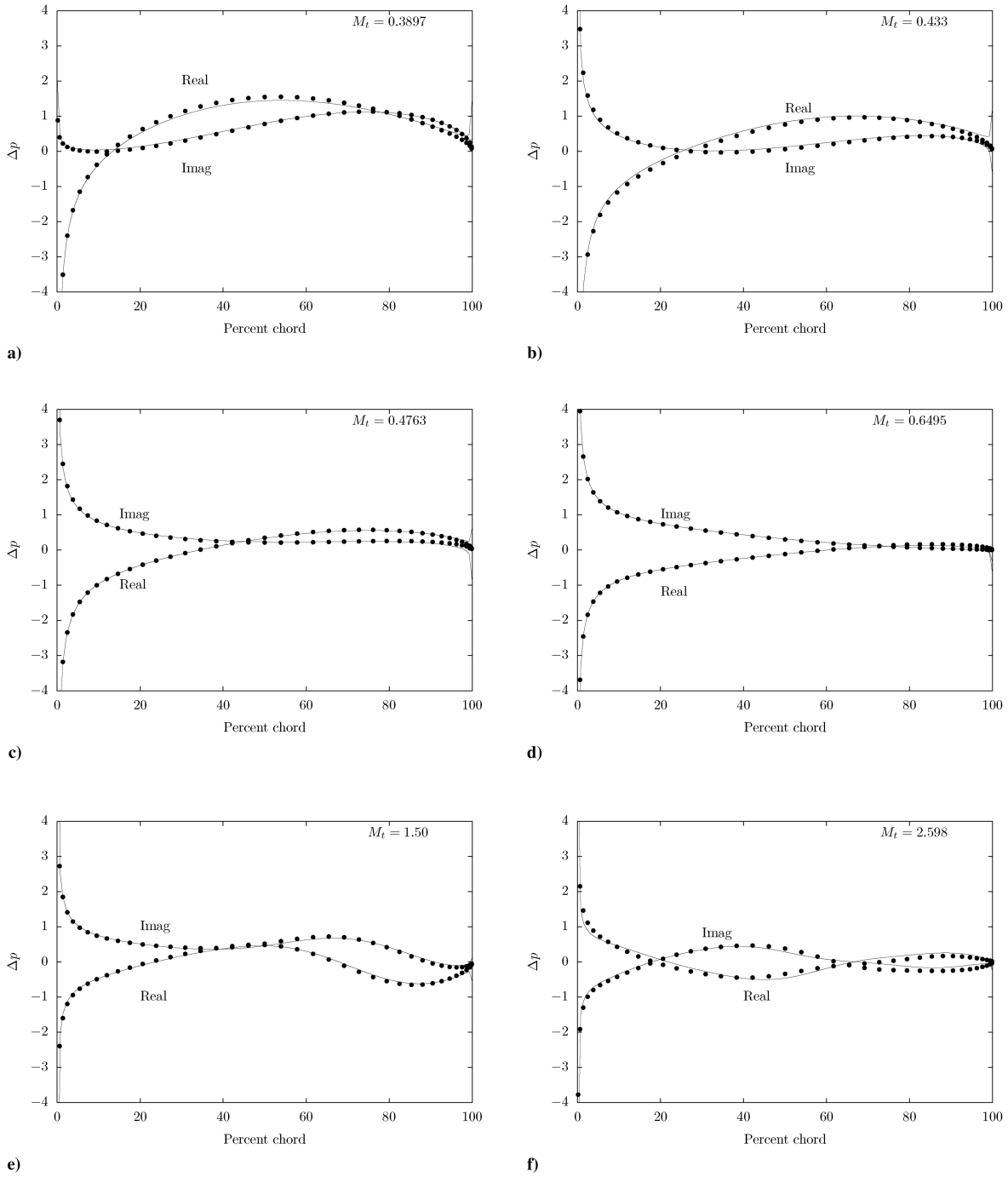

Fig. 7 Unsteady lift on a 2-D flat-plate cascade. Lines are predictions, and symbols are classical results by Smith [3].

and power levels for each downstream propagating acoustic mode are calculated. The nonreflecting boundary condition decomposes the perturbation field at the exit boundary into incoming and outgoing waves and retains only the outgoing waves. The outgoing and nondecaying acoustic modes are then used along with Eqs. (1) and (2) to calculate the integrated sound pressure (SPL) and power (PWL) levels:

$$\mathrm{SPL} = 10\log_{10}\left(\frac{1}{r_T^2 - r_H^2}\sum_{m,n}|a_{m,n}|^2\int_{r_H}^{r_T}|\psi_{m,n}|^2 r\,\mathrm{d}r\right) - 10\log_{10}(P_{\mathrm{ref}}^2) \tag{1}$$

where r_H and r_T are the hub and tip radii of the annular duct; m and n are, respectively, the circumferential and radial numbers of the propagating acoustic modes; $\psi_{m,n}$ and $a_{m,n}$ are the eigenmode and

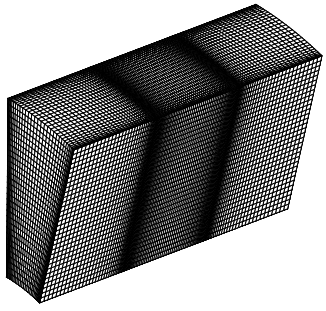

Fig. 8 Grid used to calculate the gust response of a three-dimensional flat-plate cascade. Every other point is omitted for clarity.

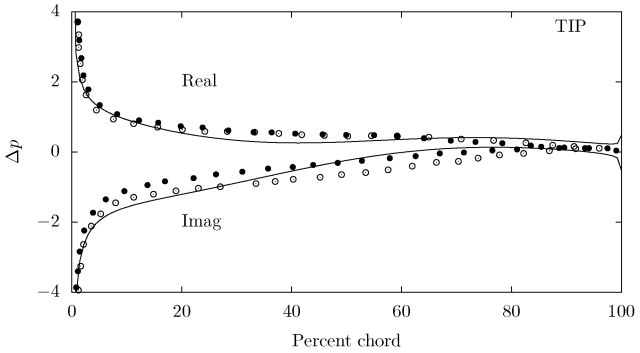

a) Span = 100%

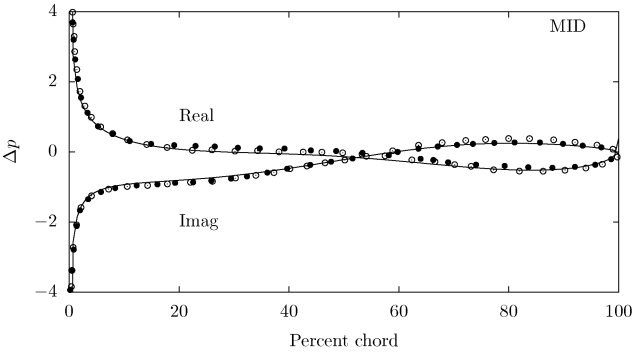

b) Span = 50%

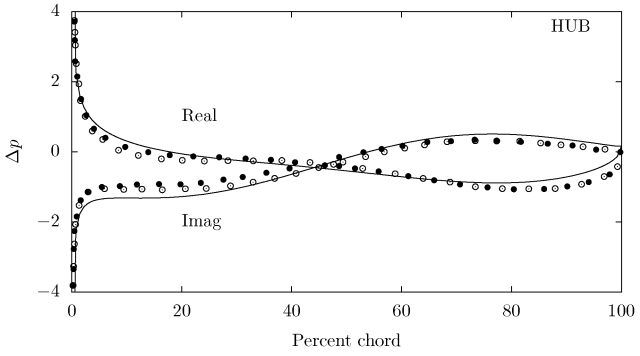

c) Span = 0%

Fig. 9 Unsteady lift at three spanwise locations of a 3-D flat-plate cascade. Lines are predictions, filled circles are results from Namba [4], and hollow circles are results from Schulten [5].

the mode amplitude, respectively, corresponding to the (m, n) mode; and $P_{\text{ref}} = 20\ \mu$ Pa is the reference acoustic pressure.

$$\text{PWL} = 10\log_{10}\left(\pi Re\left\{\sum_{m,n}|a_{m,n}|^2\int_{r_H}^{r_T}\psi^{(a)}_{m,n}(\psi^{(b)}_{m,n})^* r\,\mathrm{d}r\right\}\right) - 10\log_{10}(\text{PWL}_{\text{ref}}) \tag{2}$$

where $\psi^{(a)}_{m,n}$ and $\psi^{(b)}_{m,n}$ are the eigenmodes corresponding to the quantities $\bar{\rho}^{-1}(p' + \bar{\rho}\bar{v}_z v'_z)$ and $\bar{\rho}v'_z + \rho'\bar{v}_z$, respectively, and $\text{PWL}_{\text{ref}} = 10^{-12}$ W is the reference power level. Note that the summation in Eqs. (1) and (2) is performed over the propagating acoustics modes only.

III. Validation Against Semi-Analytical Results

In this section, validation of the prediction process against semi-analytical results for two benchmark problems [14,15] is presented. The interaction of a vortical gust with a zero-stagger flat-plate cascade is solved in two and three spatial dimensions to predict the unsteady loading on the blades.

The gust may be represented generally by

$$\mathbf{v}' = \sum_{n=1}^{\infty}\mathbf{v}'_n\exp\{inN_B(-\Omega t + k_z z + \theta + \phi)\} \tag{3}$$

where N_B is the number of rotor blades, Ω is the shaft rotation rate, ϕ is the phase, and n is the harmonic number. For a gust convecting with a uniform mean flow velocity $\bar{v}_z$, the axial wave number, k_z, is equal to $\Omega/\bar{v}_z$. The radial dependence of the gust must satisfy the solenoidal constraint $\nabla\cdot\mathbf{v}' = 0$. Following Prasad and Verdon [10], the gust is defined as

$$(v'_{n_r}, v'_{n_\theta}, v'_{n_z})^T = a_n\bar{v}_z(0, 1, -\bar{v}_z/\Omega r)^T \tag{4}$$

where a_n is the complex amplitude of the gust, and Ω is varied by changing the tip Mach number, $M_t = \Omega r_T/c$, of the rotor, where r_T is the tip radius and c is the speed of sound. The rotor and stator blade counts, N_B and N_V, respectively, determine the interblade phase angle, $\sigma = -2\pi nN_B/N_V$. Only the $n = 1$ case is presented here, and the parameter values are listed in Table 1.

A. Gust Response of a Two-Dimensional Flat-Plate Cascade

A narrow-annulus flat-plate cascade is used to approximately simulate a 2-D case for comparison against results from Smith's analysis [3]. The hub-to-tip ratio for the simulated geometry is 0.98. The grid used for the simulations is shown in Fig. 5. Six different cases are considered with parameters given in Table 2. Figure 6 compares the imaginary part of unsteady pressure in the cascade, and Fig. 7 compares the unsteady lift on the cascade. The agreement between the numerical results and Smith's results [3] is good.

B. Gust Response of a Three-Dimensional Flat-Plate Annular Cascade

Figure 8 shows the grid used for the numerical simulations of the 3-D flat-plate annular cascade. The tip radius is 3.8197, the hub-to-tip radius ratio is 0.5, and $M_t = 0.783$. Semi-analytical results for this case were presented by Namba and Schulten [5]. Figure 9 presents a comparison of the unsteady lift on the blade at three spanwise locations: 100, 50, and 0%. The results are in good agreement with the semi-analytical results. More variation is observed at the tip and hub than at the midspan section.

IV. Comparison Against NASA Source Diagnostics Test Data

The SDT is a comprehensive experimental study of the aerodynamics and acoustics of a representative high-bypass-ratio fan stage. One of the goals of the SDT study was to determine the factors affecting the generation of fan-tone noise due to the interaction of the fan rotor wake with the outlet guide vanes. Aerodynamic and acoustic measurements were taken for various rotor and stator

Table 3 Rotor design parameters

Rotor	No. of blades	Hub/tip radius ratio	Leading-edge sweep, deg	Design tip speed, m/s	Fan weight flow, lbm/s	Stage total pressure ratio
R4	22	0.3	0	370	100.5	1.47
M5	22	0.3	0	411	102.5	1.50

Table 4 Stator design parameters

	Span location	NOM	LVC	LN
Aspect ratio	Pitch line	3.51	1.67	1.67
Chord, in.	Pitch line	1.57	3.26	3.26
	Hub	2.25	2.40	2.47
Solidity	Pitch line	1.52	1.51	1.53
	Tip	1.23	1.20	1.22
	Hub	12.56	14.85	13.36
Stagger, deg	Pitch line	10.29	10.68	10.75
	Tip	10.65	10.58	11.68
	Hub	38.40	44.20	45.47
Camber, deg	Pitch line	34.56	37.57	36.06
	Tip	40.49	43.00	39.16
	Hub	0.0707	0.0707	0.0638
$t_{\max}/c$	Pitch line	0.0702	0.0702	0.0640
	Tip	0.0698	0.0698	0.0639

Table 5 Rotor speed parameters

Condition	RPM	Percent speed	Tangential tip speed, m/s
Approach	7809	61.7	228.6
Cutback	11075	87.5	324.0
Takeoff	12657	100	370.3

Table 6 SDT cases chosen for validation

Case no.	Rotor	OGV	Operating condition	Harmonic (×BPF)
1a	R4	NOM	Takeoff	1
1b	R4	NOM	Takeoff	2
2a	R4	NOM	Cutback	1
2b	R4	NOM	Cutback	2
3a	R4	NOM	Approach	1
3b	R4	NOM	Approach	2
4a	R4	LVC	Takeoff	1
4b	R4	LVC	Takeoff	2
5a	R4	LVC	Cutback	1
5b	R4	LVC	Cutback	2
6a	R4	LVC	Approach	1
6b	R4	LVC	Approach	2
7a	R4	LN	Takeoff	1
7b	R4	LN	Takeoff	2
8a	R4	LN	Cutback	1
8b	R4	LN	Cutback	2
9a	R4	LN	Approach	1
9b	R4	LN	Approach	2

geometry configurations and operational speeds. Two rotor and three stator geometries were tested in the SDT. The three stator geometries were nominal (NOM), low vane count (LVC), and low noise (LN). The design parameters for the rotor and stator are outlined in Tables 3 and 4, respectively. Only the R4 rotor is considered in this study. The rotor speed parameters are outlined in Table 5. Further details about the rotor geometry and aerodynamic performance are available in [16].

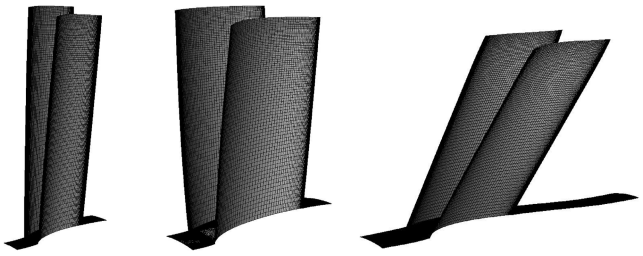

a) NOM **b) LVC** **c) LN**

Fig. 10 Grids used for acoustics calculations for the SDT cases.

Table 7 Distances between computational boundaries and vane leading/trailing edges normalized by pitch line chord

OGV	Span location	Inlet to leading edge	Trailing edge to exit
NOM	Hub/tip	0.45	0.45
LVC	Hub/tip	0.25	0.30
LN	Hub	0.58	1.50
LN	Tip	1.70	0.55

A subset of the experimental results was selected to validate the proposed prediction method. This included the R4 rotor with all three stator configurations. For each stator configuration, calculations were performed for the approach, cutback, and takeoff rotor speeds and at the first and second blade-passing frequencies. This gives a total of 16 cases (the nominal stator is cut off at the first BPF except at the takeoff condition). These are listed in Table 6.

Figure 10 shows the grids used to perform the acoustic calculation. The typical grid size used for the acoustic simulations is of the order of 4×10^6 cells. Further refinement of the grid had an insignificant effect on the acoustic results. The grid is clustered near the leading edge to accurately capture the wake interaction with the vane. The inlet and the exit boundaries are chosen to be very close to the blade (see Table 7) for two reasons. First, the wake from the rotor calculation is obtained at the inlet of the OGV computation domain. If this plane is far away from the vane leading edge, the viscous dissipation of the wake, which is not captured in the linearized inviscid analysis, will introduce a large error. Second, a smaller domain allows densely packed grids to improve spatial resolution. The proximity of the inlet and exit boundaries can lead to spurious reflections, but the high-fidelity, 3-D nonreflecting boundary condition is expected to minimize that error. A possible approach to eliminate the error from the inviscid wake evolution is to decompose the wake at the leading edge of the vane and then "unwind" the gust to the inlet of the computational domain in an inviscid fashion to ensure that the vane effectively sees the desired "viscous" gust in the linearized calculation.[‡] This approach is, however, not employed here.

Comparisons against the SDT experimental data are presented in three parts. First, the unsteady vane surface pressure is compared for one of the cases (case 6a in Table 6). Second, the exhaust modal power levels are analyzed. And last, geometric trends in the exhaust power levels are examined.

A. Vane Unsteady Pressure

The SDT vane unsteady pressure measurements were reported by Envia [1]. Measurements were made for seven fan tip speeds for the LVC and LN vanes. Pressure transducers were embedded inside the vanes and were exposed to both sides of the airfoil to measure the pressure difference between the suction and pressure sides. The suction side was taped in another set of measurements to measure the pressure fluctuations on the pressure side alone. In the discussion below, Δp refers to the pressure difference between the pressure and suction sides.

Figure 11 compares the spanwise distribution of the unsteady pressure magnitude and phase at 20% chord for case 6a. The comparison is plotted using SPLs based on root mean square pressures following the plots by Envia [1]. A qualitative match is observed, although the magnitude is underpredicted at all locations except near the casing. It is encouraging to see that the phase variation along the span is captured accurately. It is important to capture the radial phasing correctly because it determines the coupling between the aerodynamic excitation and the acoustic duct modes. The agreement with the data is, in general, better for pressure side comparisons than for Δp comparisons.

[‡]Private communication with E. Envia, 2007.

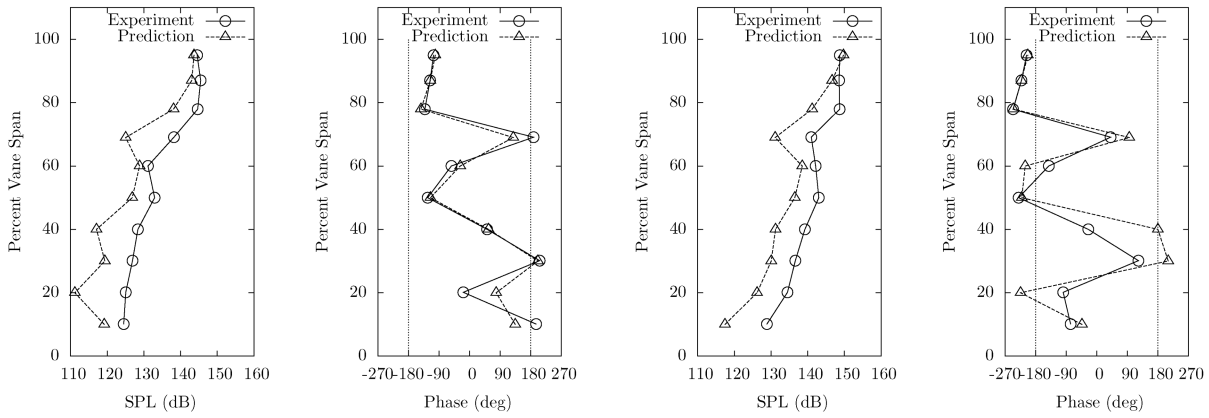

a) Pressure side b) Δp

Fig. 11 Spanwise distribution of unsteady surface pressure magnitude and phase at 20% chord for case 6a.

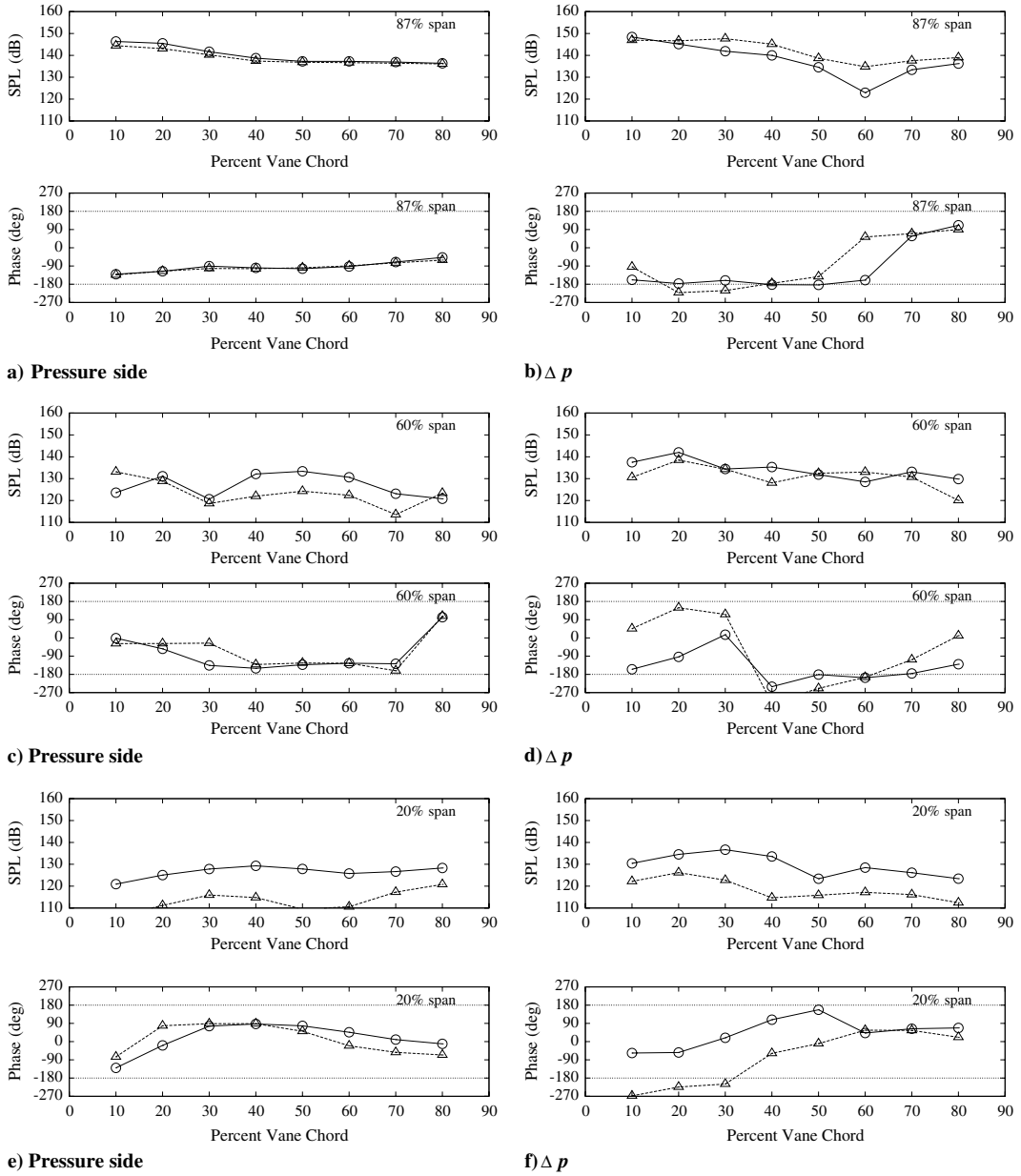

a) Pressure side b) Δp

c) Pressure side d) Δp

e) Pressure side f) Δp

Fig. 12 Chordwise distribution of unsteady pressure and phase at three span locations for case 6a. Solid lines with circles are experiments, and dashed lines with triangles are predictions.

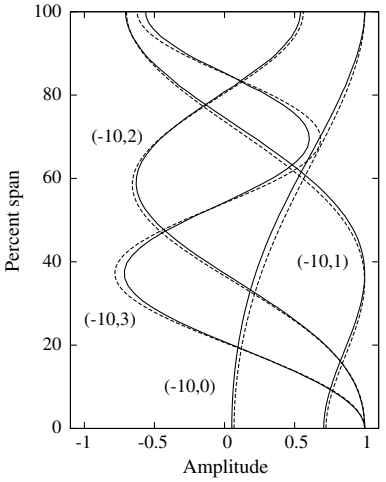

Fig. 13 First four cut-on acoustic radial modes for case 3b. Solid lines represent modes calculated using nonuniform mean flow, and dashed lines represent modes calculated by assuming uniform mean flow.

Figure 12 shows chordwise distributions of the vane unsteady pressure at three spanwise locations: −80, 67, and 20%. The predictions are qualitatively in agreement but low in magnitude in comparison to the data. Also, the agreement appears to be much better near the tip than at the hub.

B. Exhaust Tone Noise

The perturbation field at the exit boundary of the acoustic computation domain is decomposed into upstream and downstream travelling acoustic modes and convected modes, as described in the Appendix. The downstream propagating (nondecaying) acoustic modes are assumed to propagate to the duct exit without any scattering (i.e., uniform cross-sectional, coannular duct assumption). The in-duct sound power levels are compared against SDT measurement using this assumption.

The following points should be borne in mind when analyzing these comparisons. First, the NASA SDT in-duct modes are assumed to be Tyler–Sofrin [17] modes. This is true only when the mean flow is uniform. On the contrary, the acoustic modes in the predictions are calculated over the nonuniform mean flow that is present at the exit boundary of the acoustic domain. The difference due to this discrepancy should be small because the OGV removes most of the flow swirl, and the flow behind the OGV is fairly uniform. This is exemplified in Fig. 13, in which the acoustic modes predicted by the two methods described earlier are compared. Second, the cross-sectional area of the duct continuously varies from the OGV trailing edge to the exit of the nozzle, which alters the acoustic modes because of a change in duct geometry as well as the resulting change in mean flow. This alteration can be described as a scattering of energy into different modes, which is not accounted for in the present work. This effect is also expected to be small because the duct area changes only moderately over this distance.

The modal power in the test data [18] is obtained by a least-squares fit of the measured pressure projected onto the cut-on acoustics modes predicted by the Tyler–Sofrin theory [17]. In the predictions, an inner product of the perturbation field with the left eigenvector of a mode gives the amplitude of that mode. The radially integrated sound pressure and power levels are then calculated using this amplitude with Eqs. (1) and (2).

The circumferential modes expected for a given rotor–stator configuration are given by the relation $m = nN_B + kN_V$, where N_B and N_V are the numbers of rotor blades and stator vanes, respectively; n is the BPF harmonic number; and k is any integer. For example, for

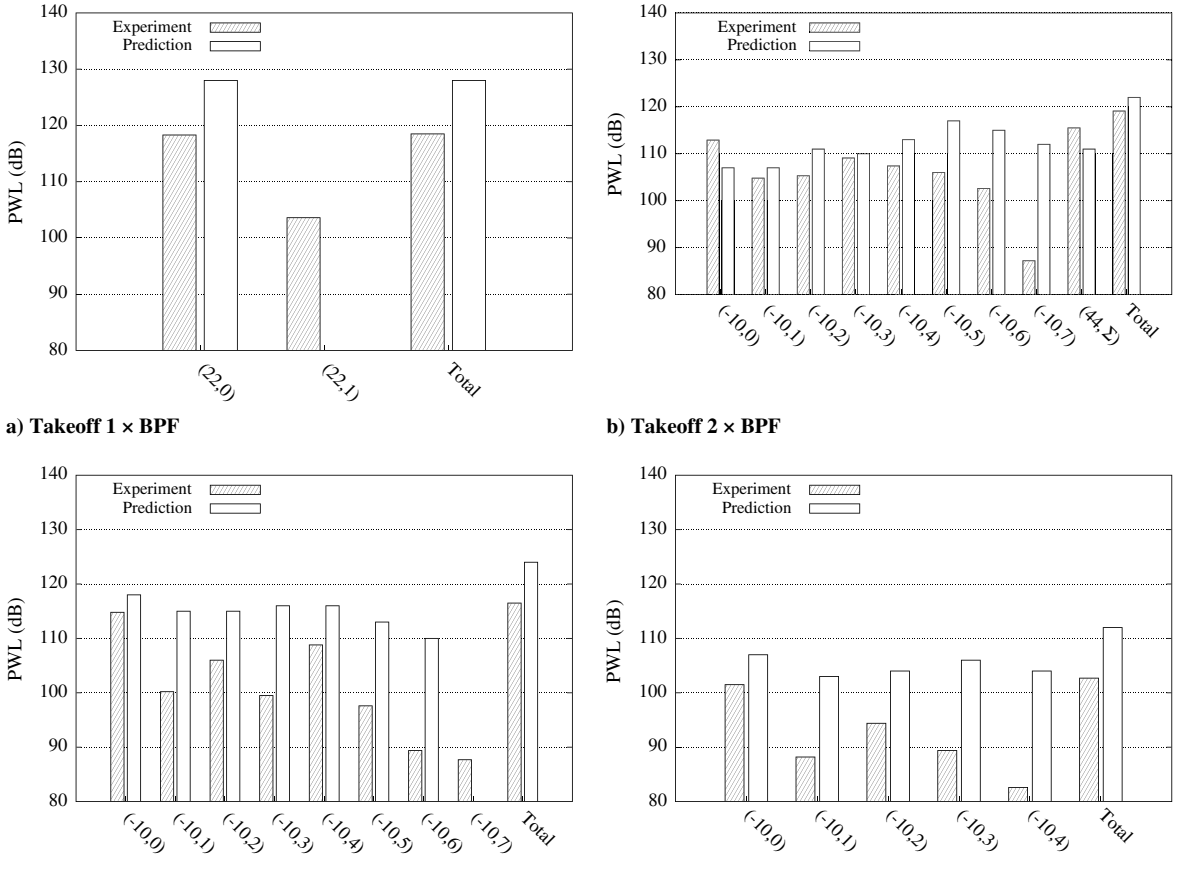

a) Takeoff 1 × BPF

b) Takeoff 2 × BPF

c) Cutback 2 × BPF

d) Approach 2 × BPF

Fig. 14 Modal results for nominal OGV configuration at takeoff, cutback, and approach conditions.

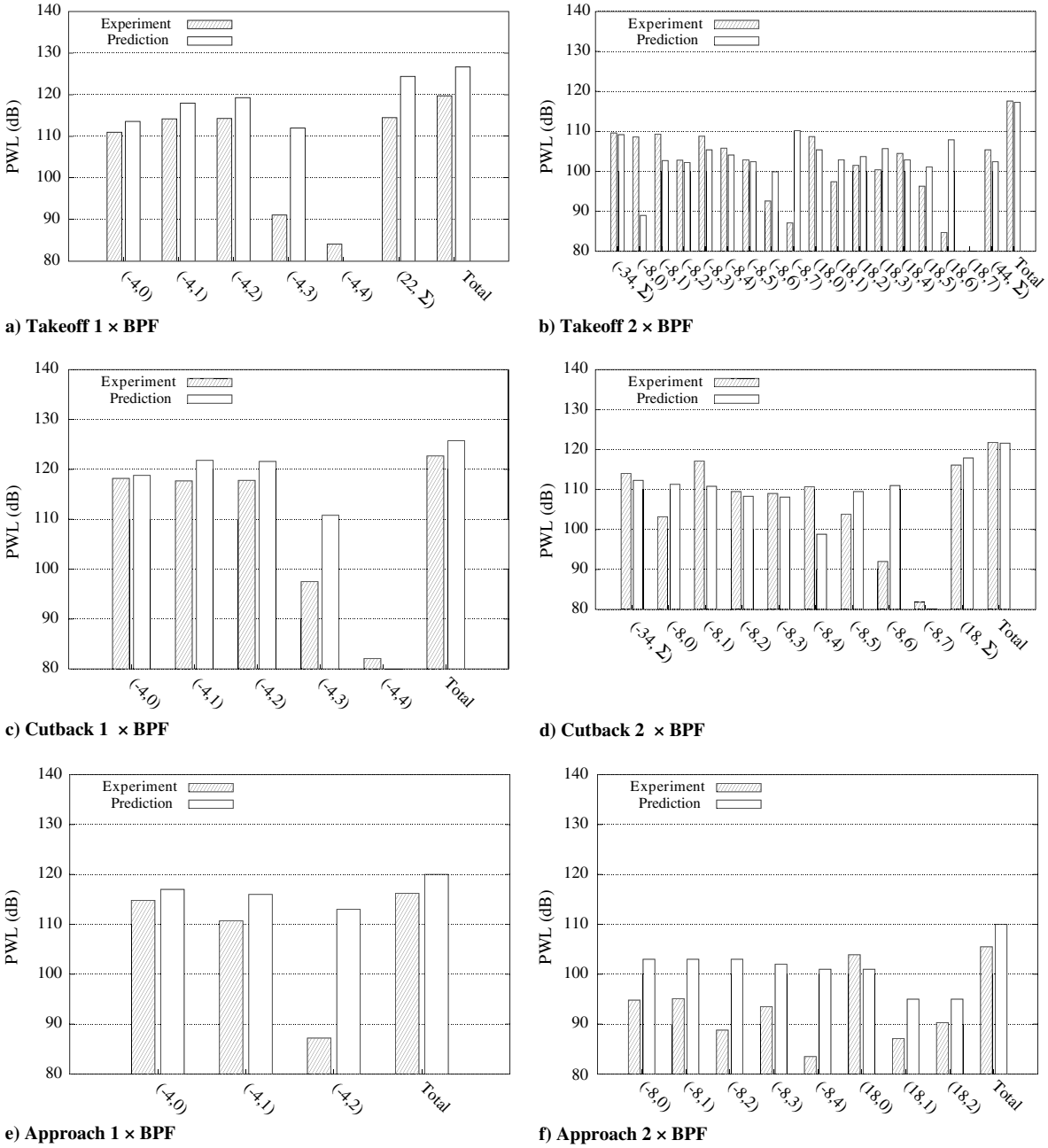

a) Takeoff 1 × BPF

b) Takeoff 2 × BPF

c) Cutback 1 × BPF

d) Cutback 2 × BPF

e) Approach 1 × BPF

f) Approach 2 × BPF

Fig. 15 Modal results for LVC OGV configuration at takeoff, cutback, and approach conditions.

a nominal vane at the second BPF, the circumferential modes that can be present are $2 \times 22 + (-1) \times 54 = -10$, $2 \times 22 + (0) \times 54 = 44$, and so on. The mode corresponding to $k = 0$ is a rotor-locked mode but is still due to the rotor–stator interaction. It is not part of the rotor-alone "self" noise, although the rotor-alone field can coexist with this tone, especially upstream of the rotor.

Figures 14–16 compare the predicted total and modal in-duct acoustic power levels with the SDT measurements for all the cases listed in Table 6. The total exhaust acoustic power is compared in the last two bars of the histograms. The BPF tone for the nominal geometry is cut off at the cutback and approach conditions; therefore, Fig. 14 presents only the second BPF results for these cases. Several acoustic modes are cut on for some cases. Therefore, for clarity, the radial modes corresponding to the higher circumferential modes for such cases are summed up and plotted using the $\sum$ symbol in the histogram plots.

The predictions capture the modal distribution quite well. The total power levels seem to be consistently overpredicted for all cases, and the average error is observed to be about 5.5 dB. The overprediction in mode power levels is rather surprising considering that the vane surface pressure comparisons show (see Fig. 11) that unsteady pressure is underpredicted. The reason for this inconsistency and for mode power overprediction is uncertain. Erroneously high wake harmonic amplitudes and the inviscid flow approximation could be two reasons for the overprediction.

C. Geometric Trends

Quantitative comparisons are a good measure of absolute prediction accuracy. However, trend predictions are of particular interest for design capability. In the SDT, there are two geometric trends: 1) effect of sweep (from LVC to LN), and 2) effect of a reduced number of vanes (from NOM to LVC). Figure 17 presents a comparison of the experiments and predictions of geometric trends at the takeoff, cutback, and approach conditions. A comparison is made for individual harmonics as well as total exhaust noise levels.

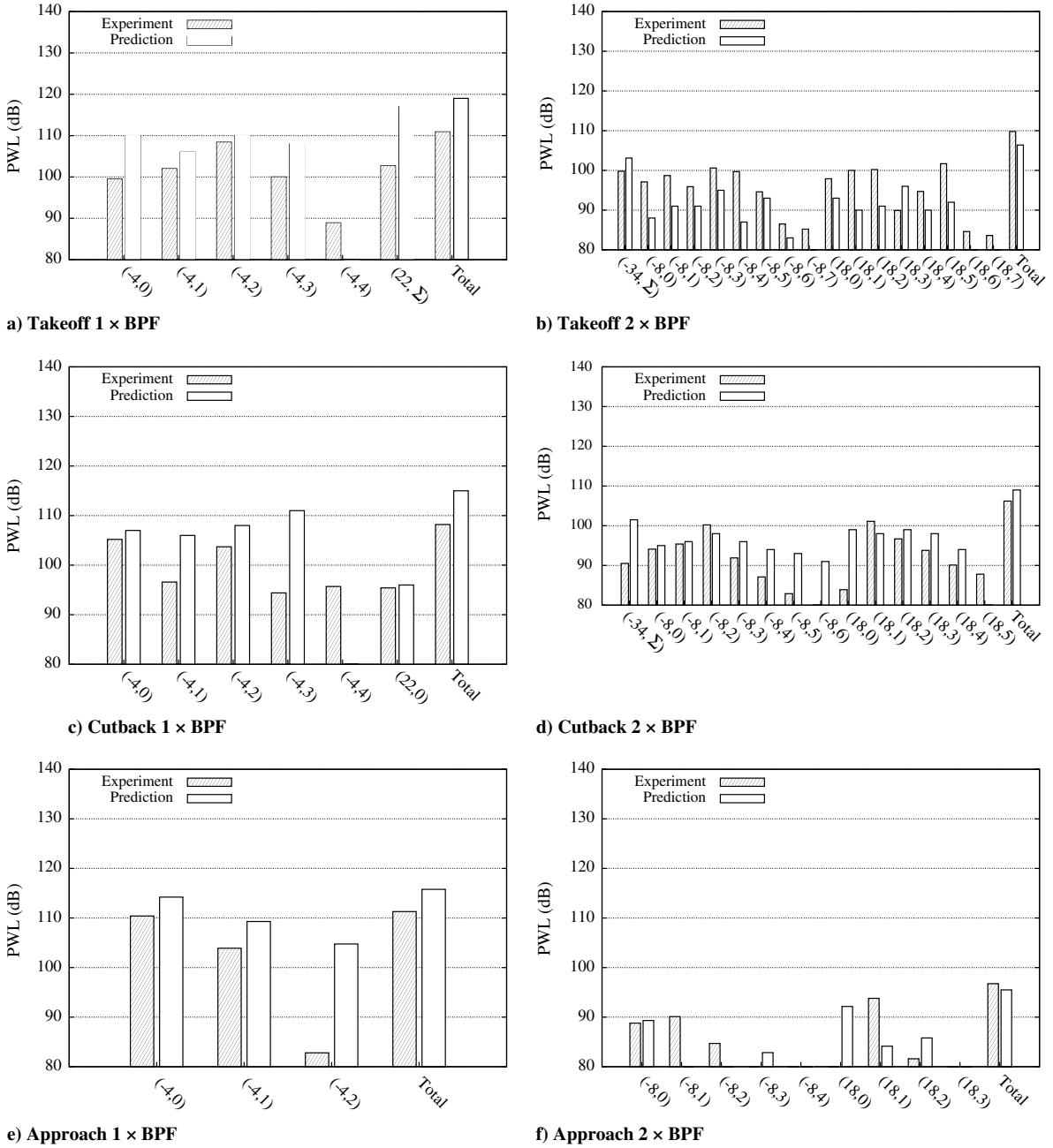

a) Takeoff 1 × BPF

b) Takeoff 2 × BPF

c) Cutback 1 × BPF

d) Cutback 2 × BPF

e) Approach 1 × BPF

f) Approach 2 × BPF

Fig. 16 Modal results for LN OGV configuration at takeoff, cutback, and approach conditions.

The benefit of sweep in reducing interaction noise is well known [7,19]. Sweep introduces additional spanwise phase variation in the gust and, consequently, in the unsteady loading on the vane. This reduces the total acoustic power when pressure perturbation is integrated over the span. Also, higher spanwise phasing enhances the coupling of unsteady lift on the blade with higher radial order modes (which are more cut off), thereby reducing noise. The benefit of sweep for noise reduction can be clearly seen in Fig. 17 by focusing on trend lines from LVC to LN. The effect of sweep is well captured by the numerical results.

The effect of reduced vane count (NOM to LVC trend) on fan-tone noise is more complicated. Any change in blade count has to be accompanied by a change in the blade chord to maintain the blade solidity. This is required to maintain the same aerodynamic performance of the machine. The LVC OGV in SDT, which has only 26 blades, has a wider chord than the NOM vane, which has 54 blades. The reduction in vane count is a direct reduction in the number of noise sources, which is beneficial for noise reduction. Also, the wide chord blade effectively sees a lower reduced frequency (defined using blade chord) than the nominal blade, which again reduces noise (Sear's function [20]). However, with the reduction in vane count the unsteady loading on each vane goes up, which generates more noise. Furthermore, the reduction in the number of vanes permits lower-order circumferential modes in the duct, which are more efficient at radiating acoustic energy. The net radiated noise is a sum of all these effects, and the resulting trends can be confounding.

The biggest penalty of reducing the number of vanes below a threshold (two times the number of rotor blades) is that the first BPF gets cut on for the cutback and approach conditions in addition to takeoff. The effect of this on overall noise can be seen in Figs. 17f and 17i. The large increase in noise from NOM to LVC is due to the first BPF tone, which is only present for the LVC geometry. The vane count reduction is, however, beneficial in reducing the rotor–stator interaction broadband noise [21].

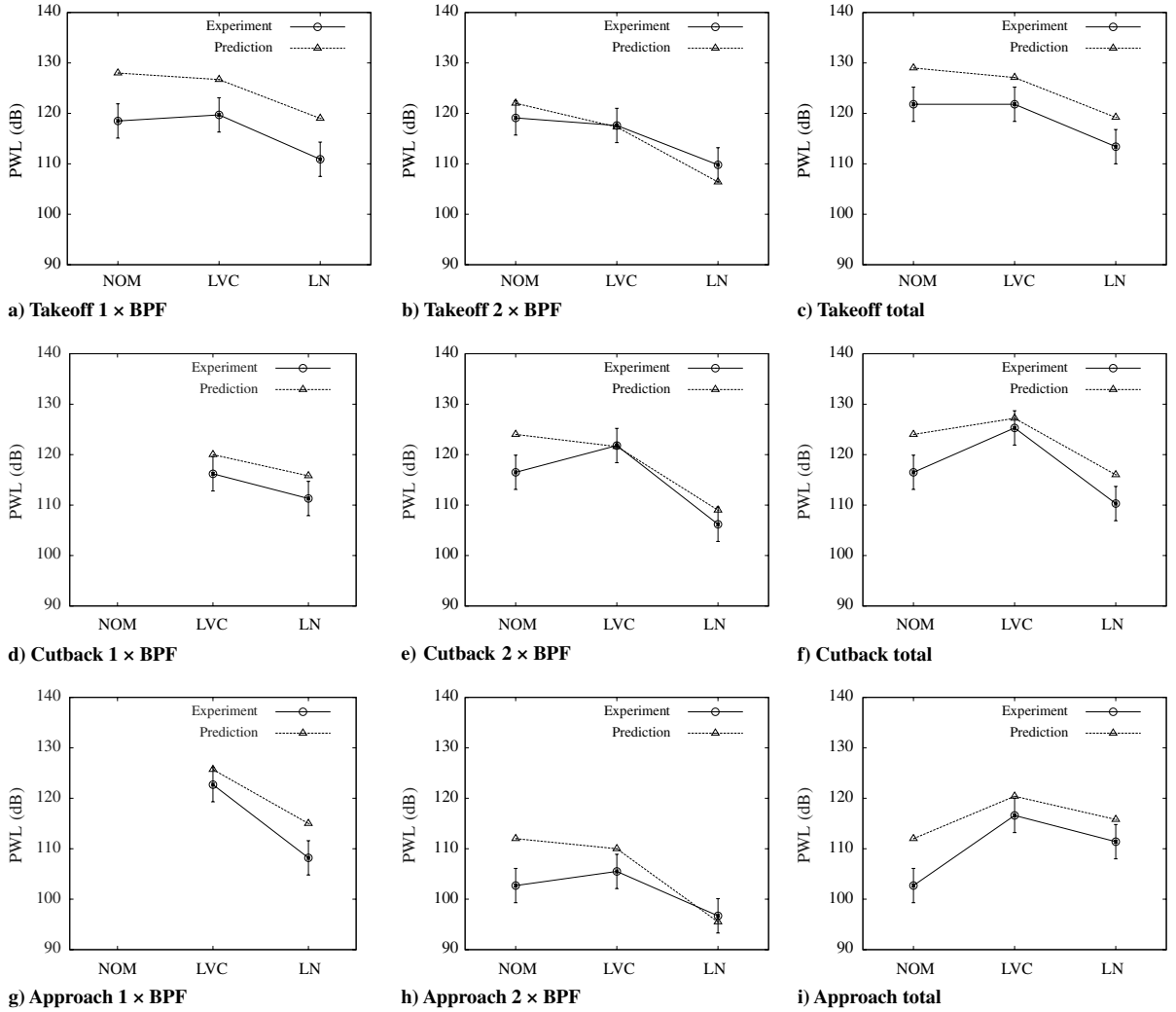

Fig. 17 Comparison of geometry trends.

V. Conclusions

A prediction methodology for fan-tone noise simulations has been described. The process has been validated against canonical cases in which the agreement with semi-analytical results is found to be very good. A detailed comparison against the NASA Source Diagnostic Test data has been performed for vane unsteady pressure and in-duct exhaust noise levels. The capability of the process to predict geometric trends has also been verified against the SDT data. The average error has been observed to be about 5.5 dB, with the numerical results being consistently higher than the data for acoustic power.

Appendix: Formulation of the Three-Dimensional Nonreflecting Boundary Conditions

The linearized Euler equations in cylindrical coordinates are

$$\frac{\partial \mathbf{U}'}{\partial t} + \frac{1}{r}\frac{\partial}{\partial r}(r\bar{A}\mathbf{U}') + \frac{1}{r}\bar{B}\frac{\partial \mathbf{U}'}{\partial \theta} + \bar{C}\frac{\partial \mathbf{U}'}{\partial z} - \bar{D}\mathbf{U}' = 0 \qquad \text{(A1)}$$

where

$$\mathbf{U}' = \begin{Bmatrix} \rho' \\ v_r' \\ v_\theta' \\ v_z' \\ p' \end{Bmatrix}$$

and the matrices $\bar{A}$, $\bar{B}$, $\bar{C}$, and $\bar{D}$ expressed in primitive variables are

$$\bar{A} = \begin{pmatrix} \bar{v}_r & \bar{\rho} & 0 & 0 & 0 \\ 0 & \bar{v}_r & 0 & 0 & \frac{1}{\bar{\rho}} \\ 0 & 0 & \bar{v}_r & 0 & 0 \\ 0 & 0 & 0 & \bar{v}_r & 0 \\ 0 & \gamma\bar{p} & 0 & 0 & \bar{v}_r \end{pmatrix}, \quad \bar{B} = \begin{pmatrix} \bar{v}_\theta & 0 & \bar{\rho} & 0 & 0 \\ 0 & \bar{v}_\theta & 0 & 0 & 0 \\ 0 & 0 & \bar{v}_\theta & 0 & \frac{1}{\bar{\rho}} \\ 0 & 0 & 0 & \bar{v}_\theta & 0 \\ 0 & 0 & \gamma\bar{p} & 0 & \bar{v}_\theta \end{pmatrix}$$

$$\bar{C} = \begin{pmatrix} \bar{v}_z & 0 & 0 & \bar{\rho} & 0 \\ 0 & \bar{v}_z & 0 & 0 & 0 \\ 0 & 0 & \bar{v}_z & 0 & 0 \\ 0 & 0 & 0 & \bar{v}_z & \frac{1}{\bar{\rho}} \\ 0 & 0 & 0 & \gamma\bar{p} & \bar{v}_z \end{pmatrix}$$

$$\bar{D} = \begin{pmatrix} 0 & 0 & 0 & 0 & 0 \\ \frac{(\bar{v}_\theta+\Omega r)^2}{\bar{\rho}r} & 0 & \frac{2(\bar{v}_\theta+\Omega r)}{r} & 0 & \frac{1}{\bar{\rho}r} \\ -\frac{\bar{v}_r(\bar{v}_\theta+2\Omega r)}{\bar{\rho}r} & -\frac{(\bar{v}_\theta+2\Omega r)}{r} & -\frac{\bar{v}_r}{r} & 0 & 0 \\ 0 & 0 & 0 & 0 & 0 \\ 0 & \frac{(\gamma-1)\bar{\rho}(\bar{v}_\theta+\Omega r)^2}{r} & -\frac{(\gamma-1)\bar{\rho}\bar{v}_r(\bar{v}_\theta+2\Omega r)}{r} & 0 & -\frac{(\gamma-1)\bar{v}_r}{r} \end{pmatrix} \qquad \text{(A2)}$$

In Eq. (A2), the overbar denotes a mean flow quantity, and the prime denotes a perturbation quantity.

Assuming a wave solution of the following form:

$$\mathbf{U}'(r,\theta,z,t) = \sum_{m=-\infty}^{\infty}\sum_{n=-\infty}^{\infty} \hat{\mathbf{U}}'_{mn}(r)e^{j(-\omega t+m\theta+k_z z)} \qquad \text{(A3)}$$

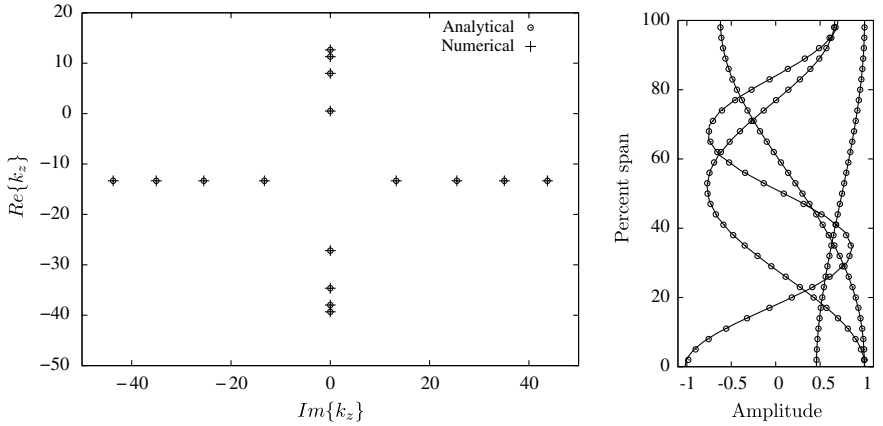

a) Eigenvalues **b) Eigenvectors**

Fig. A1 Validation of the numerical eigensystem solution against the analytical results. In Fig. A1b, lines are the analytical results and circles are the numerically computed results.

and substituting into Eq. (A1) gives

$$-j\omega\hat{\mathbf{U}}'_{mn}+\frac{1}{r}\frac{\partial}{\partial r}(r\bar{A}\hat{\mathbf{U}}'_{mn})+j\frac{m}{r}\bar{B}\hat{\mathbf{U}}'_{mn}+jk_z\bar{C}\hat{\mathbf{U}}'_{mn}-\bar{D}\hat{\mathbf{U}}'_{mn}=0 \tag{A4}$$

The radial derivative term in the Eq. (A4) can be represented using a numerical differential operator (using either spectral or finite differencing) as

$$\frac{1}{r}\frac{\partial}{\partial r}(r\bar{A}\hat{\mathbf{U}}'_{mn})=\mathcal{L}_r\hat{\mathbf{U}}'_{mn} \tag{A5}$$

Substituting into Eq. (A4) yields the following eigensystem:

$$[-j\omega I+\mathcal{L}_r+j(m/r)\bar{B}+jk_z\bar{C}-\bar{D}]\hat{\mathbf{U}}'_{mn}=0 \tag{A6}$$

Because of the numerical representation of the radial operator, this eigensystem must be solved numerically. The numerical solution of the system generally contains some spurious modes, in addition to acoustic and convective modes. A convected mode simply convects downstream with the mean flow and can be identified by comparing its group velocity, $V_{g,mn}$, with the local mean flow velocity. The group velocity can be calculated using the relation

$$V_{g,mn}=\frac{\partial\omega}{\partial k_z}=\frac{\langle\mathbf{L}_{mn},\bar{C}\mathbf{R}_{mn}\rangle}{\langle\mathbf{L}_{mn},\mathbf{R}_{mn}\rangle} \tag{A7}$$

where k_z is the eigenvalue, and L_{mn} and R_{mn} are the left and right eigenvectors of Eq. (A6). After filtering out the spurious and the convected modes from the solution, the acoustic perturbation solution can be written as

$$\mathbf{U}'(r,\theta,z,t)=\sum_{m=-\infty}^{\infty}\sum_{n=-\infty}^{\infty}a_{mn}\mathbf{R}_{mn}(r)e^{j(-\omega t+m\theta+k_z z)} \tag{A8}$$

The eigensystem solution is verified by comparing the eigenvalues and eigenvectors against the analytical solution for acoustic modes in an annular duct with uniform mean flow. A sample comparison is provided in Fig. A1.

The acoustic waves can be grouped into left- and right-running waves. The direction of the evanescent waves (nonzero imaginary value of k_z) is determined by the sign of $\mathrm{Im}\{k_z\}$ (the magnitude of $\mathrm{Im}\{k_z\}$ determines the decay rate) and that of the propagating (nondecaying) waves is determined by the direction of the group velocity. The amplitudes of the incoming/outgoing acoustic modes from a boundary are obtained by taking an inner product of the perturbation field at the boundary, with $\mathbf{U}'$ given by Eq. (A8) for the incoming/outgoing direction. At the nonreflecting boundaries, only the outgoing characteristics are used to compute the auxiliary cell values. In addition, the incoming characteristics of the excitation are imposed in the auxiliary cells at the boundary where the excitation is specified.

The nonreflecting-boundary-condition implementation is verified by comparing the predictions against the analytical solutions for canonical problems. Two independent simulations are carried out with a purely vortical wave and a purely acoustic wave specified at the inlet of an annular duct with a nonzero ($M=0.5$) mean flow. The vortical wave is specified using Eq. (4), and the acoustic wave is

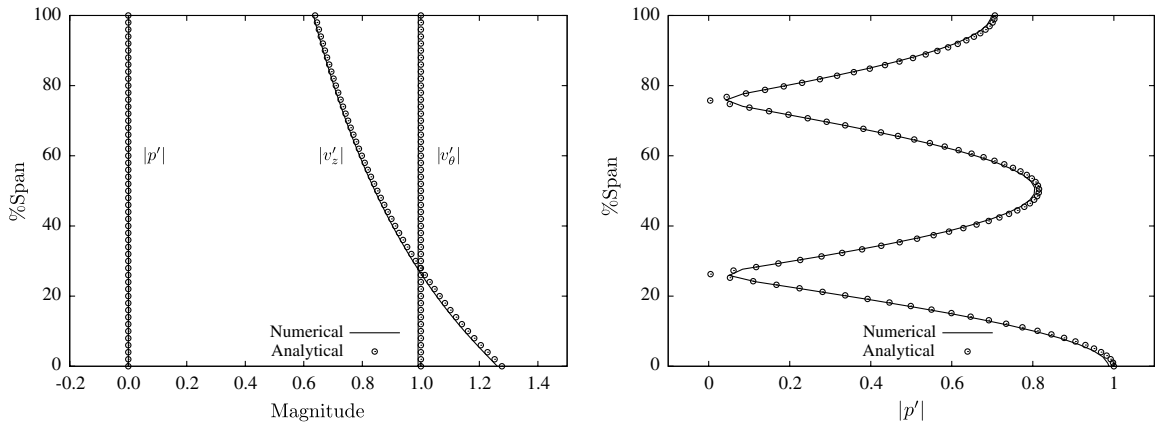

a) Vortical wave **b) Acoustic wave**

Fig. A2 Comparison of the numerical and analytical solutions at the exit boundary of the computational domain in an annular duct with a uniform mean flow.

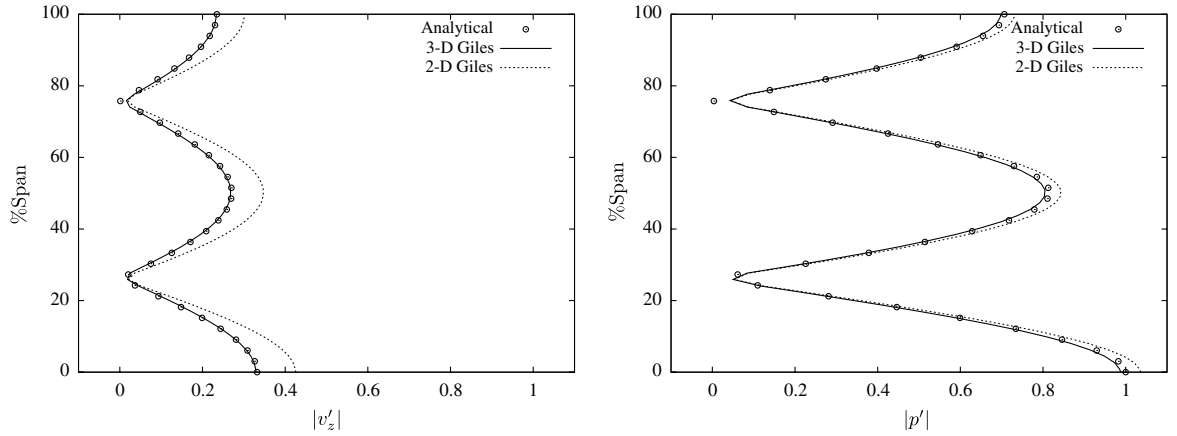

a) $|v_z'|$ **b)** $|p'|$

Fig. A3 Comparison of the numerical solutions (at the computational exit boundary) using 3- and 2-D Giles nonreflecting boundary conditions against the analytical solution.

specified to be the hard-wall duct mode $(m, n) = (1, 2)$ with unit amplitude. The vortical wave should convect downstream with no change in amplitude. The acoustic wave also travels through the duct unchanged, as it is driven at a frequency higher than the cutoff frequency. The numerical solution at the exit boundary of the computational domain is compared against the analytical solution in Fig. A2. As can be seen, the match between the analytical solution and the numerical calculation is very good, indicating that the boundary condition is nonreflective.

The 3-D nonreflecting boundary conditions are also compared against 2-D Giles boundary conditions for the case of an acoustic mode traveling in a duct [22]. The comparison is presented in Fig. A3. Although the comparison of acoustic pressure in Fig. A3 is acceptable with the 2-D Giles boundary condition, the corresponding v_z' is quite severely overpredicted; this would result in an overprediction of the acoustic power of the mode.

Acknowledgments

The authors would like to thank General Electric Aviation for providing financial support to carry out this research and for granting permission to publish the results presented here. The authors also gratefully acknowledge colleagues Richard Cedar, John Wojno, and Gregory Szczepkowski (General Electric Aviation), and Edmane Envia (NASA John H. Glenn Research Center at Lewis Field) for many fruitful discussions on the subject.

References

[1] Envia, E., "Fan Noise Source Diagnostic Test—Vane Unsteady Pressure Results," NASA TM 2002–211808, 2002.

[2] Verdon, J., "Linearized Unsteady Aerodynamic Analysis of the Acoustic Response of Wake/Blade-Row Interaction," NASA CR–2001-210713, 2001.

[3] Smith, S. N., "Discrete Frequency Sound Generation in Axial Flow Turbomachines," Aeronautical Research Council Rept. 3709, 1973.

[4] Namba, M., "Three-Dimensional Analysis of Blade Force and Sound Generation for an Annular Cascade in Distorted Flows," *Journal of Sound and Vibration*, Vol. 50, No. 4, 1977, pp. 479–508. doi:10.1016/0022-460X(77)90498-9

[5] Namba, M., and Schulten, J. B. H. M., "Numerical Results of Lifting Surface Theory," *Third Computational Aeroacoustics Workshop on Benchmark Problems*, CP 2000-209790, NASA, Washington, D.C. 2000, pp. 73–85.

[6] Schulten, B. H. M., "Sound Generated by Rotor Wakes Interacting with a Leaned Vane Stator," *AIAA Journal*, Vol. 20, 1982, pp. 1352–1358. doi:10.2514/3.51195

[7] Schulten, B. H. M., "Vane Sweep Effects on Rotor/Stator Interaction Noise," *AIAA Journal*, Vol. 35, No. 6, 1997, pp. 945–951. doi:10.2514/2.198

[8] Whitehead, D. S., "A Finite Element Solution of Unsteady Two-Dimensional Flow in Cascades," *International Journal for Numerical Methods in Fluids*, Vol. 10, No. 1, 1990, pp. 13–34. doi:10.1002/fld.1650100103

[9] Hall, K. C., and Verdon, J. M., "Gust Response Analysis for Cascades Operating in Nonuniform Mean Flows," *AIAA Journal*, Vol. 29, No. 9, 1991, p. 1463. doi:10.2514/3.10761

[10] Prasad, D., and Verdon, J. M., "A Three-Dimensional Linearized Euler Analysis of Classical Wake/Stator Interactions: Validation and Unsteady Response Predictions," *International Journal of Aeroacoustics*, Vol. 1, No. 2, pp. 137–163. doi:10.1260/147547202760236941

[11] Atassi, H. M., Ali, A. A., and Atassi, O. V., "Interaction of Acoustic and Vortical Disturbances with an Annular Cascade in a Swirling Flow," *Unsteady Aerodynamics, Aeroacoustics and Aeroelasticity of Turbomachines*, edited by K. C. Hall, R. E. Kielb, and J. P. Thomas, Springer, Berlin/New York/Heidelberg, 2003, pp. 247–259.

[12] Atassi, H. M., Ali, A. A., Atassi, O. V., and Vinogradov, I. V., "Scattering of Incident Disturbances by an Annular Cascade in a Swirling Flow," *Journal of Fluid Mechanics*, Vol. 499, 2004, pp. 111–138. doi:10.1017/S0022112003007031

[13] Envia, E., Huff, D. L., and Morrison, C. R., "Analytical Assessment of Stator Sweep and Lean in Reducing Rotor-Stator Tone Noise," AIAA Paper 1996-1791, 1996.

[14] Dahl, M. D. (ed.), *Third Computational Aeroacoustics (CAA) Workshop on Benchmark Problems*, CP–2000-209790, NASA, Washington, DC, 2000, pp. 16–20.

[15] Dahl, M. D. (ed.), *Fourth Computational Aeroacoustics (CAA) Workshop on Benchmark Problems*, CP–2004-212954, NASA, Washington, DC, 2004, pp. 59–65.

[16] Hughes, C. E., Jeracki, R. J., Woodward, R. P., and Miller, C. J., "Fan Noise Source Diagnostic Test—Rotor Alone Aerodynamic Performance Results," NASA TM 2005–211681, 2005.

[17] Tyler, J. M., and Sofrin, T. G., "Axial Flow Compressor Noise Studies," *SAE Transactions*, Vol. 70, 1962, pp. 309–332.

[18] Heidelberg, L. J., "Fan Noise Source Diagnostic Test—Tone Modal Structure Results," NASA TM–2002-211594, 2002.

[19] Woodward, R., Elliot, D. M., Hughes, C. E., and Berton, J. J., "Benefits of Swept and Leaned Stators for Fan Noise Reduction," NASA TM 1998–208661, 1998.

[20] Sears, W. R., "Some Aspects of Non-Stationary Airfoil Theory and Practical Applications," *Journal of the Aeronautical Sciences*, Vol. 8, No. 3, 1941, pp. 104–188.

[21] Ganz, U. W., Joppa, P. D., Patten, T. J., and Scharp, D. F., "Boeing 18-Inch Fan Rig Broadband Noise Test," NASA CR-1998-208704, 1998.

[22] Giles, M., "Nonreflecting Boundary Conditions for Euler Equation Calculations," *AIAA Journal*, Vol. 28, 1990, pp. 439–461. doi:10.2514/3.10412,

[23] Goldstein, M. E., *Aeroacoustics*, McGraw–Hill, New York, 1976.

C. Bailly
Associate Editor